ESTIMATING CONCENTRATIONS OF FINE-GRAINED AND TOTAL SUSPENDED SEDIMENT FROM CLOSE-RANGE REMOTE SENSING IMAGERY

Adam R. Mosbrucker, Kurt R. Spicer, Tami S. Christianson, and Mark A. Uhrich,
U.S. Geological Survey, Cascades Volcano Observatory, Vancouver, Wash., amosbrucker@usgs.gov

INTRODUCTION

Fluvial sediment, a vital surface water resource, is hazardous in excess. Suspended sediment, the most prevalent source of impairment of river systems, can adversely affect flood control, navigation, fisheries and aquatic ecosystems, recreation, and water supply (e.g., Rasmussen et al., 2009; Qu, 2014). Monitoring programs typically focus on suspended-sediment concentration (SSC) and discharge (SSQ). These time-series data are used to study changes to basin hydrology, geomorphology, and ecology caused by disturbances. The U.S. Geological Survey (USGS) has traditionally used physical sediment sample-based methods (Edwards and Glysson, 1999; Nolan et al., 2005; Gray et al., 2008) to compute SSC and SSQ from continuous streamflow data using a sediment transport-curve (e.g., Walling, 1977) or hydrologic interpretation (Porterfield, 1972). Accuracy of these data is typically constrained by the resources required to collect and analyze intermittent physical samples.

Quantifying SSC using continuous instream turbidity is rapidly becoming common practice among sediment monitoring programs. Estimations of SSC and SSQ are modeled from linear regression analysis of concurrent turbidity and physical samples. Sediment-surrogate technologies such as turbidity promise near real-time information, increased accuracy, and reduced cost compared to traditional physical sample-based methods (Walling, 1977; Uhrich and Bragg, 2003; Gray and Gartner, 2009; Rasmussen et al., 2009; Landers et al., 2012; Landers and Sturm, 2013; Uhrich et al., 2014). Statistical comparisons among SSQ computation methods show that turbidity-SSC regression models can have much less uncertainty than streamflow-based sediment transport-curves or hydrologic interpretation (Walling, 1977; Lewis, 1996; Glysson et al., 2001; Lee et al., 2008). However, computation of SSC and SSQ records from continuous instream turbidity data is not without challenges; some of these include environmental fouling, calibration, and data range among sensors. Of greatest interest to many programs is a hysteresis in the relationship between turbidity and SSC, attributed to temporal variation of particle size distribution (Landers and Sturm, 2013; Uhrich et al., 2014). This phenomenon causes increased uncertainty in regression-estimated values of SSC, due to changes in nephelometric reflectance off the varying grain sizes in suspension (Uhrich et al., 2014).

Here, we assess the feasibility and application of close-range remote sensing to quantify SSC and particle size distribution of a disturbed, and highly-turbid, river system. We use a consumer-grade digital camera to acquire imagery of the river surface and a depth-integrating sampler to collect concurrent suspended-sediment samples. We then develop two empirical linear regression models to relate image spectral information to concentrations of fine sediment (clay to silt) and total suspended sediment. Before presenting our regression model development, we briefly summarize each data-acquisition method.

RIVER REMOTE SENSING

Remote sensing is a rapidly growing subdiscipline in river science due to its ability to answer complex spatial and temporal questions; cost-effective data acquisition, processing and analysis; and the increasing adoption of geospatial technology by hydrologists (Marcus and Fonstad, 2010). River remote sensing has become a broad field. Active (e.g., lidar) and passive optical (e.g., photogrammetry) remote sensing provide precise topographic measurements to assess geomorphic characteristics and sediment transport of river environments. Spectral analyses of reflected electromagnetic (EM) radiation recorded by satellite-based optical sensors have been successfully used to estimate turbidity and SSC of large rivers over a broad range of time-scales and from low to medium concentrations (e.g., Curran and Novo, 1988; Mertes et al., 1993; Islam et al., 2001; Wang et al., 2009; Wang and Lu, 2010; Wang et al., 2010; Qu, 2014).

SATELLITE SENSORS

Satellite imagery provides retrospective and spatial information about a river system. Spectral analyses of satellite imagery are based on the measurement of reflected EM solar radiation. Material properties produce unique signatures, or curves, depending on reflection and absorption of different wavelengths (λ); sensors commonly record data in the

visible to short-wave-infrared spectra. Multispectral data are recorded as pixel unit values within a multilayer array, or raster image file. Each layer, or band, is sensitive to a unique wavelength range, commonly rendered as red, green, and blue (RGB), though imagery may contain dozens of bands.

In satellite remote sensing, pixel values, generally referred to as digital numbers (DNs), are calibrated into physically meaningful units of radiance (i.e., watts per unit area). Surface reflectance spectra, derived from atmospheric correction of radiance imagery, are then used to quantify features within an image. Maximum reflectance sensitivity of clear water is near the blue end of the spectrum (λ<500 nm), reflectance decreases as wavelength increases. Turbid water, with greater SSC, has increased sensitivity toward the red end of the spectrum (λ>600 nm), accounting for its brownish appearance.

The relationship between reflectance and SSC is affected by suspended material composition, water depth, SSC variation over depth, and view geometry (Qu, 2014). Empirically-developed models relating spectra to SSC in riverine and laboratory environments use linear, second-order polynomial, and logarithmic equations (Table 1). While most utilize the near-infrared (NIR) spectrum (λ>700 nm), of interest to our study is Islam et al. (2001) who used the blue spectrum of MODIS satellite imagery (Band 3, λ=459–479 nm) to estimate SSC in the Ganges and Brahmaputra Rivers (about 400–1,800 mg/L) (Table 1). Peak response of our consumer-grade sensor is 470 nm.

Table 1 Selected empirical models predicting river suspended-sediment concentration (SSC) from satellite imagery and laboratory measurements. The values of the surface reflectance of the water at the given wavelengths (r_i) are explanatory variables in these equations (*ith* band of a given sensor). Table modified from Qu (2014).

Sensor Platform	Wavelength λ (nm)	Spatial Resolution (m)	Location	Model	R^2	Samples (n)	Reference
MODIS satellite	841-876, 1230-1250	250-500	Yangtze River (China)	$SSC = -23.03 + 60.25(r_2 - r_5) - 23.03$	0.73	153	Wang et al., 2010
		250-500	Yangtze River (China)	$ln(SSC) = 4.117 + 0.262(r_2 - r_5)$	0.78	35	Wang and Lu, 2010
Landsat satellite	760-900	30	Yangtze River (China)	$ln(SSC) = -1.40060 + 3.18263 ln(r_4)$	0.88	24	Wang et al., 2009
MODIS satellite	459-479	500	Ganges and Brahmaputra Rivers (Bangladesh)	$SSC = -201 + 69.39 r_3$	0.98	10	Islam et al., 2001
Laboratory spectrometer	852	--	Lab, silt	$SSC = -23.367 + 116.869 r_{852} + 24.04 r^2_{852}$	0.99	10	Lodhi et al., 1997
	852	--	Lab, clay	$SSC = -23.367 + 116.869 r_{852} + 24.04 r^2_{852}$	0.96	10	Lodhi et al., 1997
	555, 754	--	Lab, clay (organic)	$SSC = -0.31 + 12.32(r_{555}/r_{754})$	0.92	7	Gin et al., 2003

CONSUMER-GRADE DIGITAL CAMERA SENSORS

We expand upon previous laboratory and satellite image analyses by evaluating the feasibility of using imagery acquired with a consumer-grade digital camera at a distance <10 m above a river surface to estimate SSC. Compared to satellite-based platforms, close-range remote sensing can measure smaller streams at similar wavelengths with as much as 1,000 times greater spatial resolution, and algorithms for spectral mixing and atmospheric correction are not needed (Mertes et al., 1993; Qu, 2014). The primary differences between industrial- and consumer-grade sensors are the characteristics of individual bands (Table 2). Whereas each band of satellite imagery is sensitive to radiation within a narrow and discrete bandwidth (e.g., 20–80 nm), consumer-grade sensors have a broadband response (e.g., 200–300 nm) with significant overlap among only three bands (Table 2).

Consumer-grade sensors are sensitive to wavelengths between 200 and 1,300 nm. However, manufacturers use ultraviolet (UV) and NIR interference filters to restrict recorded EM radiation to the visible spectrum (400–700 nm) in order to more precisely focus light rays onto a single plane (Figure 1). These filters, located in front of the sensor, can be removed to restore the full spectral range of the native sensor. Apparent brightness and color measurements are typically recorded in 8-bit integer (i.e., values 0–255) Joint Photographic Experts Group (JPEG) file format, which have a defined color space, or coordinate system (e.g., sRGB, Adobe RGB, ProPhoto RGB). File format type, bit depth, and color space determine the degree of signal processing, precision, and range of data.

Table 2 Spectral response characteristics for selected satellite and consumer-grade sensors (band λ in nm). Lighter grey area is native (unfiltered) response of a Nikon D800E sensor. Where known, peak response is given in white font. A Forest Technology Systems (FTS) DTS-12 turbidity sensor (emitted λ) is included for reference purposes.

Platform	Sensor	Band No.	Range (λ, nm)	Bandwidth (λ, nm)	UV Light 300	Visible Light 400	500	600	NIR Light 700	800	900	1000	1100	1200
Terrestrial	D800E	1	380-620	240		470								
		2	380-620	240			540							
		3	380-680	300				590						
Satellite	Landsat TM[1]	1	450-520	70		510								
		2	520-600	80			590							
		3	630-690	60				650						
		4	760-900	140						880				
Satellite	MODIS[2]	1	620-670	50				▓						
		2	841-876	35						▓				
		3	459-479	20		▓								
		4	545-565	20			▓							
		5	1230-125	20										▓
In situ	DTS-12	1	780-900	120					▓					

[1]The Landsat TM sensor has three additional middle- to thermal-infrared bands (band 5−7, λ=1,550−12,500 nm). [2] The MODIS sensor has 31 additional bands (λ=450−14,385 nm). Abbreviations: ultraviolet (UV); near infrared (NIR).
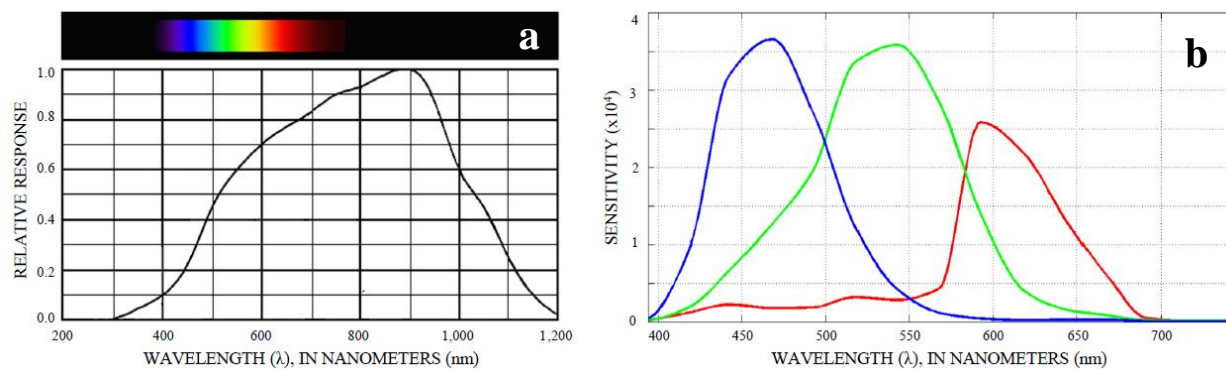

Figure 1 Spectral response curves of (a) native and (b) filtered sensor used in a Nikon D800E digital single-lens reflex (DSLR) camera. Response curves for sensors used in consumer-grade digital cameras from other manufacturers are similar. Figure modified from Profilocolore Sri (2013).

STUDY AREA

The May 18, 1980, eruption of Mount St. Helens consisted of a 2.5 km^3 debris avalanche followed by a blast density current, pyroclastic flows, lahars, and tephra falls (e.g., Lipman and Mullineaux, 1981). These disturbances severely altered the hydrogeomorphic regime of the upper North Fork Toutle River, whose 450 km^2 basin includes the north flank of the volcano. Our investigation was conducted at an existing USGS surface water discharge and suspended-sediment monitoring station, 13 river km downstream of the toe of the debris avalanche deposit (primary sediment source), and 2 river km below a sediment retention structure near Kid Valley, Washington (14240525). More than three decades after the eruption, the river continues to transport an average of 3 million tonnes (or megagrams, Mg) of suspended sediment per year; daily average SSC is 31–79,800 mg/L (water years 2007–2013). A significant portion of the annual SSQ is transported during infrequent high-streamflow events. Suspended particle sizes range from clay to sand; material is commonly 50−80% fines (i.e., <63 µm). Fines are well distributed in cross section and vertical profile. Bed material is dominantly sand. Annual mean water discharge at the station is 22.3 m^3/s (water years 1990–2013).

DATA COLLECTION AND ANALYSIS METHODS

To evaluate the feasibility of estimating suspended-sediment characteristics from close-range multispectral imagery, we developed a simple, reproducible, and effective methodology for image acquisition, sample collection, and analysis. Concurrent pairs of suspended-sediment samples and imagery were acquired during routine site visits between January and June, 2014. Data were collected over a range of hydrologic conditions and turbidity, with an emphasis on capturing high-flow events. In total, 716 photographs and 100 samples were acquired during this 6-month period. A calibration data pair consists of a series of normalized imagery and associated suspended-sediment samples.

SUSPENDED-SEDIMENT SAMPLES

Standard USGS field and laboratory methods were used for suspended-sediment sample collection and analyses (Guy, 1969; Edwards and Glysson, 1999). Suspended-sediment samples were collected using a D-74 depth-integrating sampler with a 0.48-cm-diameter brass nozzle (Edwards and Glysson, 1999; Davis et al., 2005) deployed from a bank-operated cableway. Primary samples used in the calibration dataset were collected at a single station within the camera's field of view. Secondary cross-section samples were collected using an equal discharge increment (EDI) method for future relation of results to cross-sectional mean concentrations. We collected full-depth and near-surface samples (i.e., 7 cm below the river surface), usually in two sets to assess variability (Topping et al., 2011).

Sediment analyses were performed at the USGS Cascades Volcano Observatory in Vancouver, Washington. SSC data were computed using the dry weight of all sediment from a sampled volume. Particle diameter was measured with a sieve and sedigraph. Primary samples (n=39) have wide variation in SSC (262–7339 mg/L) and particle size distribution (28–94% <63 μm; 10–33% <4 μm; 4–24% <2 μm). Root-mean-square error (RMSE) of lab results is about 4% (USGS, 2014), but sample data show a moderate to high degree of spatial and temporal variability. SSC for full-depth samples is typically <10% greater than near-surface samples and occasionally as much as 40% (due to sand in suspension near the streambed). Samples taken within a few minutes of each other in the same location have SSC values that differ by ≤25%. Particle size data show 9–30% less sand near the river surface.

CLOSE-RANGE MULTISPECTAL IMAGERY

CAMERA SYSTEM

One of the first tasks of our study was to select a camera system and develop a consistent procedure for data acquisition and analysis. We used the same camera system and configuration throughout the study. Camera sensor and lens (i.e., camera system) selection focused on optimizing spatial and spectral resolution, ability to calibrate white balance, automate exposure compensation, produce RAW image files (which have 64–256 times more brightness levels than a standard 8-bit JPEG files), select color space, and use a configuration file. Spatial resolution is a function of the sensor and the lens. Higher resolution sensors, commonly measured in megapixels (MP), combined with fixed focal length lenses (generally 35–85 mm) produce the greatest resolution; optical aberrations of lenses can have a significant impact on resolution.

Although data are widely available for spatial resolution and other image-quality parameters of consumer-grade digital camera systems, the spectral response of a specific sensor is difficult to obtain. DxO Labs, an imaging solution and standardization company, publishes image quality lab test results of digital image capture devices through their website (*http://dxomark.com*). DxOMark quantifies image quality using three resolution-normalized metrics: dynamic range, color sensitivity, and noise levels. For our purposes, we sought to maximize dynamic range and color sensitivity (or color bit-depth), while minimizing noise in an affordable off-the-shelf consumer-grade camera.

On the basis of these criteria, we chose a Nikon D800E digital single-lens reflex camera (DSLR) with a 70–300 mm focal length lens to provide flexibility. According to DxOMark lab results, this system has similar image quality to others costing as much as 10 times more. The camera uses a 864 mm^2 Sony IMX094AQP CMOS image sensor, which has 36.56 MP (4.8 μm each), a 14-bit non-linear analogue-to-digital converter (for 14.3 exposure values (EV) of dynamic range), 25.6 bits of color depth, and an ISO of 2979. The broadband sensor has a native spectral response range of 300–1250 nm, reduced to about 380–680 nm after passing through UV-NIR interference filters (Figure 1). The system allows JPEG files to be spectrally normalized through custom white balance calibration.

IMAGE ACQUISITION AND ANALYSIS

Immediately before, during, or after collecting suspended-sediment samples, we acquired multispectral imagery of the water surface at a camera station collocated at the sampling site. The camera was mounted to a handrail <5 m above the water surface at a 45° angle to maximize water surface penetration (Figure 2). The rail was marked to facilitate precise relocation of the mount. The same 70 mm focal length was used for all imagery; field of view was 28.8° horizontal and 19.5° vertical, imaging an ~8.9 m^2 frame, depending on river stage. This represents a nominal water surface sampling distance of 0.5 mm per pixel (i.e., medium- to course-sand) at the center of the field of view, which was set to the sample location, 1.5–2.1 m from the left bank (Figure 2).
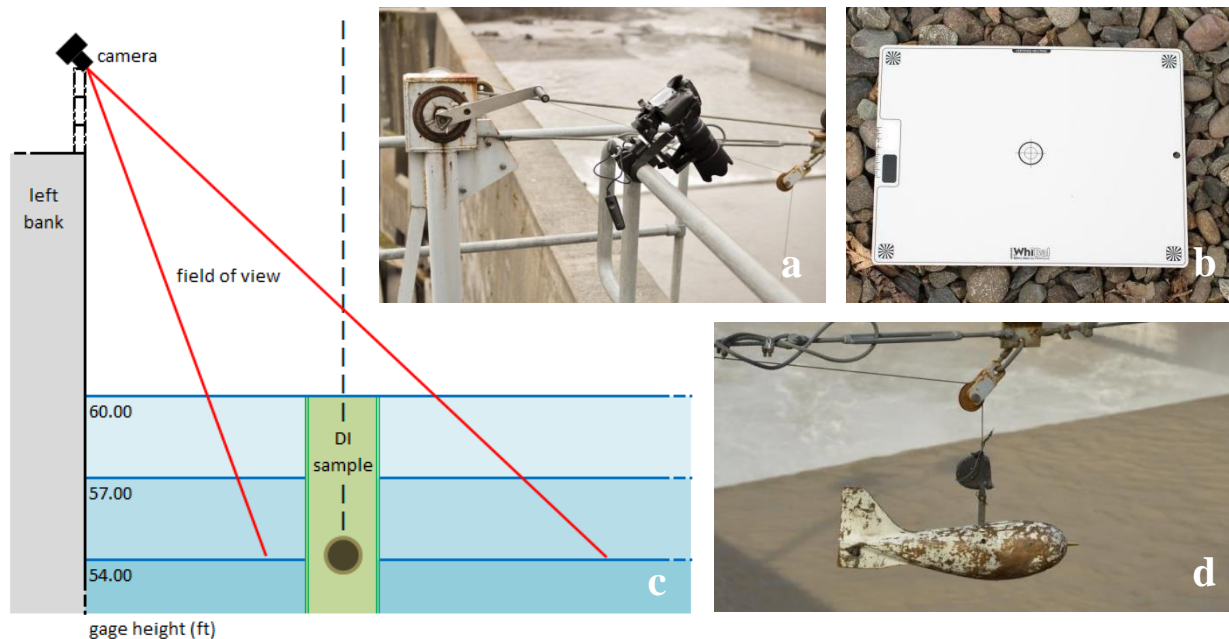

Figure 2 Field data collection panel showing (a) the camera system mounted on handrail near bank-operated cableway, (b) white balance calibration card, (c) relationship of camera field of view to suspended-sediment sample location, and (d) D-74 depth-integrated sampler deployed from the cableway. Views are downstream from left bank.

Initial methodology focused on maximizing the information capacity of each dataset, because we did not know what would prove to be most useful. Datasets consisted of three sequences of nine exposure-bracketed images (0.3–1.0 EV intervals) at a high frame rate (Figure 3). Each sequence used a different glass lens filter (clear, ultraviolet, polarized) to modify the water surface reflectance prior to sensor detection. To account for changing ambient lighting conditions, each sequence was normalized by a calibrated white balance target (Figure 2b). Camera settings optimized image quality at the expense of file size and shutter speed; a configuration file was used to ensure consistent in-camera processing settings. Consistent image acquisition proved challenging in some conditions, such as rapidly changing ambient light or presence of woody debris (drift) within the field of view. These were mitigated by acquiring additional bracketing sequences at wider EV intervals to prevent limited dynamic range from clipping the sensor output values. Sand boils on the river surface, which cause irregular dark patches, were common and could not be avoided.

A total of 15 datasets were collected during our initial investigation (Table 3). The limited scope of this study prevented comprehensive image analysis; we explored only a few spectral indices, file format conversions, and signal processing filters (e.g., low-pass). We sought to evaluate the use of a standard-precision file format (8-bit JPEG), medium-resolution color space (Adobe RGB), normal EV, and test the sensitivity among lens filters.

Each image file is comprised of three spectral bands within the visible spectrum; RGB (Red, 380–680 nm; Green, 380–680 nm; Blue, 380–620 nm). Due to the broadband response of the sensor, we focused our analysis on the peak of the response curve for each band (Red, 590 nm; Green, 540 nm; Blue, 470 nm). Descriptive statistic were computed

from uncalibrated, but spectrally normalized, DNs (pixel values) for each band as well as the average of all three bands; statistics included minimum, maximum, mean, standard deviation (1-sigma), and covariance.

Figure 3 Typical 10-frame dataset showing white balance reference card (WB) and -4 to +4 exposure value (EV) bracketing sequence. This example was acquired during diffuse (overcast) ambient lighting conditions.

CALIBRATION DATASET

A calibration dataset compiled image statistics and sample lab results. Imagery and suspended-sediment samples were paired by time of acquisition; time differences between images and physical samples were limited to ≤30 minutes for all pairs. Mean time difference for the dataset is 11 minutes. Samples were then grouped by near-surface, full-depth, and combined sample depths. All samples were analyzed for SSC and a subset for particle size distribution. We selected three representative size classes (<63 µm, <4 µm, and <2 µm) and computed mass concentrations from total SSC.

Table 3 Calibration dataset summary table. Sample total suspended-sediment concentration (SSC) is given as well as concentration of material finer than 63 µm (SSC$_{fines}$). Six SSC samples were excluded due to significantly different times (i.e., >30 minutes) between image acquisition and sample collection.

Date	Dataset	Imagery		Suspended Sediment Samples			Turbidity		Streamflow (m^3/s)
		(n)	EV[1]	(n)	SSC (mg/L)	SSC$_{fines}$ (mg/L)	Trend[2]	FNU[3]	
1/6/2014	1	27	8.0	3	368	220	Fall	73	16.4
	2	27	8.0	1	262	192	Fall	62	16.8
1/11/2014	3	54	8.0	3	4664	2955	Rise	890	69.1
	4	54	8.0	2	5424	3713	Rise	1840	73.6
	5	27	2.6	2	6535	4905	Peak	3380*	72.8
2/12/2014	6	54	8.0	2	2325	1415	Peak	870	53.8
	7	74	8.0	1	1989	1357	Fall	820	53.8
	8	99	8.0	4	1668	942	Fall	570	51.0
3/6/2014	9	54	2.6	4	6765	3520	Trough	3840*	91.2
	10	36	2.6	2	6885	6183	Rise	4170*	92.3
	11	54	2.6	4	6661	6027	Fall	4160*	97.7
3/7/2014	12	54	5.4	4	5154	4409	Fall	2520	78.4
4/22/2014	13	27	5.4	3	929	338	Trough	66	33.1
	14	18	5.4	1	1182	329	Rise	78	32.0
6/6/2014	15	57	5.4	3	367	256	Fall	140	13.5

[1]Exposure value (EV) is the range of illuminance, as referenced to the camera exposure meter. For instance, a dataset with an exposure-bracketed sequence of -4 to +4 EV has a range of 8 EV. [2]Trend of turbidity is based on 15-minute unit values whereas sample collection took <5 minutes. [3]Turbidity is recorded using a Forest Technology Systems DTS-12 sensor in Formazin Nephelometric Units (FNU) (Anderson, 2005). Values exceeding the sensor maximum (1,850 FNU, denoted by an * in the table) are recorded from a Hach Solitax sensor in Formazin Backscatter Ratio Units (FBRU).

EMPIRICAL REGRESSION MODELS

Relationships between imagery, suspended-sediment concentration, and particle size were investigated using ordinary least squares regression. We used simple linear regression (SLR) to describe the covariability of these variables and evaluate the ability to predict suspended-sediment information from spectral measurements of a river surface. Statistical methods described in Helsel and Hirsch (2002) were used to develop and evaluate our models.

We began investigating the relationship between possible explanatory (x) and response (y) variables by generating a correlation matrix for our entire calibration dataset. From these results, we modeled the most highly correlated variables to evaluate the quality of fit and significance of the relationship. More specifically, we checked for non-linearity, heteroscedasticity (i.e., non-constant variability of residuals), and the coefficient of determination (R^2). Full-depth and near-surface samples were evaluated both individually and combined. From these exploratory data analyses, we found the explanatory variable B_{max} (maximum DN, or pixel value, of the blue band) using a clear lens filter to be most related to SSC and particle size response variables. Concentration of material smaller than sand (<63 µm, SSC_{fines}) was of greatest interest; other particle size classes were weakly correlated. We developed two SLR models: one for total SSC and another for SSC_{fines} response variables based on the B_{max} explanatory variable using combined full-depth and near-surface samples. Both models benefited from base-10 logarithmic transformation to achieve linearity, homoscedasticity, and normality of residuals (Helsel and Hirsch, 2002). Base-10 transformation, or equivalent power function regression, is common among turbidity-SSC regression and streamflow-SSC transport curves (e.g., Glysson, 1987; Curtis et al., 2006; Rasmussen et al., 2009; Uhrich et al., 2014).

CORRELATION OF IMAGERY TO SUSPENDED-SEDIMENT CONCENTRATION

Our final SLR model predicting SSC from B_{max} DN shows a statistically significant relationship between the two variables (t-statistic and p-value at 95% confidence interval; Figure 4 and Table 4). The model explains 90% of the variability in sampled SSC (R^2; Table 4). Probability plot correlation coefficient (PPCC, R^2=0.87) indicates that residuals have a homoscedastic pattern and near-normal distribution (Helsel and Hirsch, 2002; Rasmussen et al., 2009). The $\log_{10}$-transformed model is:

$$\log_{10}(SSC) = 12.707 - 4.225\log_{10}(B_{max}), \tag{1}$$

where

SSC	is suspended-sediment concentration (mg/L), and
B_{max}	is the maximum uncalibrated pixel value, in DN (8-bit, 0<x<255).

The $\log_{10}$-transformed SLR model (equation 1) can be retransformed and corrected for associated bias, resulting in:

$$SSC = (5.0933 \times 10^{12})(B_{max}^{-4.225}) \times BCF, \tag{2}$$

where

BCF	is a nonparametric bias correction factor.

It should be noted that Duan's smearing bias correction factor (BCF) (Duan, 1983) is a best estimate of the bias introduced by retransforming regression estimates to the original units (e.g., SSC in mg/L), computed using the average of residuals (e.g., Uhrich and Bragg, 2003; Rasmussen et al., 2009; Uhrich et al., 2014). The bias correction factor for equation 2 was determined to be 1.0461, yielding a final SLR model:

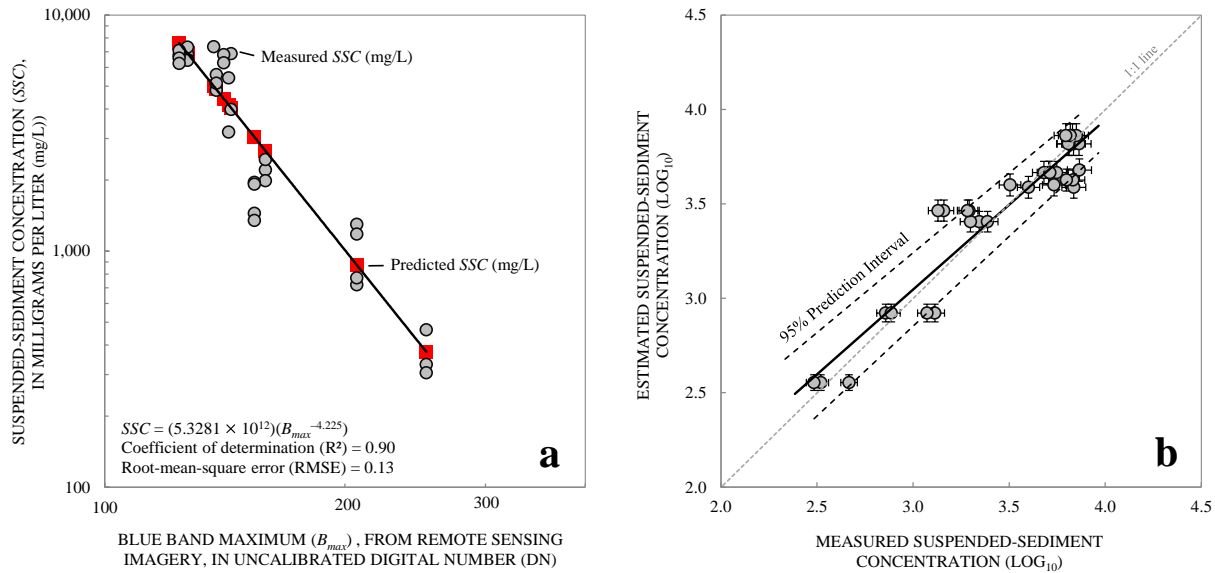$$SSC = (5.3281 \times 10^{12})(B_{max}^{-4.225}). \tag{3}$$

Figure 4 Results of simple linear regression (SLR) analysis using $\log_{10}$-transformed data for (a) spectra and suspended-sediment concentration (SSC) data, and (b) comparison of measured and estimated SSC in log space with 95% prediction interval and 5% error bars on measured concentration. Standard errors of intercept and slope are 0.560 and 0.256 respectively.

Table 4 Regression model summary with statistical diagnostics and analysis of variance (ANOVA). A multivariate regression model for the North Fork Toutle River station is shown for comparison purposes (Uhrich et al., 2014).

Response (*y*)	Explanatory (*x*)		Model	Obs. (*n*)	Conc. (mg/L)	R^2	RMSE	MSPE	Coefficient SE	t-statistic	p-value
SSC	B_{max}		$\log_{10}(SSC) = 12.707 - 4.225\log_{10}(B_{max})$	33	305–7339	0.90	0.133	26.4–35.8	0.256	- 16.53	6.29E-17
SSC_{fines}	B_{max}		$\log_{10}(SSC_{fines}) = 14.484 - 5.111\log_{10}(B_{max})$	33	250–6438	0.90	0.163	31.3–45.6	0.314	- 16.29	9.43E-17
SSC			$\log_t(SSC) = -0.8054 + 0.1854\log_t T +$	653	30–10100	0.81	0.228			
	T	turbidity	$0.3545\log_t Tlag + 0.8952\log_t Q$						0.2882	0.64	0.52
	Q	discharge							0.2897	1.22	0.221
	$Tlag$	lag T value							0.04497	19.91	0.
	t	15-minute interval time									

Abbreviations: Coefficient of determination (R^2); model standard percentage error (MSPE); coefficient standard error (SE).

CORRELATION OF IMAGERY TO CONCENTRATION OF SUSPENDED OF FINES

The final SLR model predicting concentration of fine material in suspension (<63 µm) shows a statistically significant relationship that explains 90% of the concentration variability (R^2; Figure 5 and Table 4). Normality of residuals was significantly improved by logarithmic transformation (PPCC, R^2=0.90). The $\log_{10}$-transformed model is:

$$\log_{10}(SSC_{fines}) = 14.484 - 5.111\log_{10}(B_{max}), \tag{4}$$

where

SSC_{fines} is concentration of fine material (<63 µm) in suspension.

Retransformation of equation 4 with an associated *BCF* of 1.0675 yields a final SLR model in exponential form:

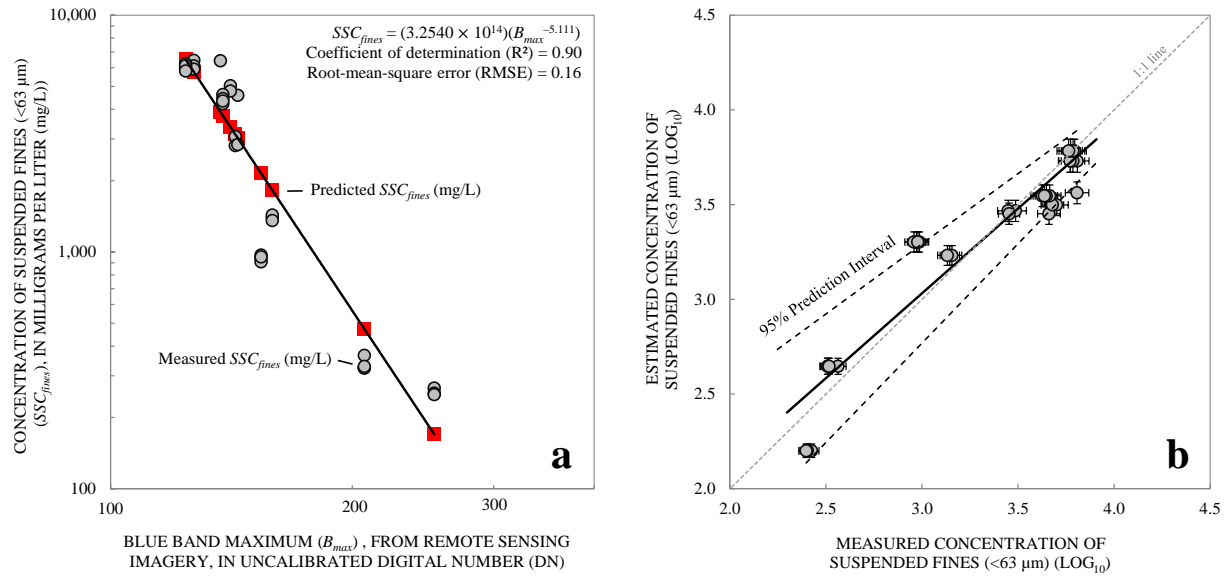$$SSC_{fines} = (3.2540 \times 10^{14})(B_{max}^{-5.111}). \tag{5}$$

Figure 5 Results of simple linear regression (SLR) analysis using $\log_{10}$-transformed data for (a) spectra and concentration of suspended fines (SSC_{fines}) data, and (b) comparison of measured and estimated SSC_{fines} in log space with 95% prediction interval and 5% error bars on measured concentration. Standard errors of intercept and slope are 0.687 and 0.314 respectively.

DISCUSSION AND FUTURE STUDIES

Our results show that uncalibrated DNs (pixel values) extracted from RGB imagery of a river surface can be used as the explanatory variable in a SLR model to predict SSC (R^2=0.90). Modeled SSC values are -126% to 41% different than sampled SSC, with a mean error of -10%. The satellite-based spectral reflectance signature of turbid water is well established, with a positive correlation of the near-infrared (NIR) spectrum (λ>700 nm) to SSC. Because unmodified consumer-grade digital camera sensors are weakly sensitive to red and near-infrared wavelengths, we use the peak response of the UV-blue end of the spectrum (B_{max}, λ=470 nm), which yields a negative correlation (i.e., negative slope of regression line). Our finding makes logical sense; color saturation of a river's opaque brownish appearance increases as SSC in the river increases. In this situation, the response near the red spectra increases while the blue spectra decreases.

Expanding upon this result, we show that the same SLR explanatory variable (B_{max}) can be used to predict SSC_{fines} (R^2=0.90). This is not surprising, given that the response variables SSC and SSC_{fines} are strongly correlated (i.e., SSC_{fines} $\propto$ SSC) for our data (fines average 3,204 mg/L or 72% of total suspended mass). Modeled SSC_{fines} error is -136% to 39% with a mean of -15%. Like the previous model, the regression line has a negative slope; opacity of water is largely a function of fines concentration. Given that the absorption of EM energy by water is the weakest in the blue spectra (i.e., greatest depth penetration), we expected B_{max} to be better correlated to SSC_{fines} than SSC. Our results show the SSC model is slightly better than the SSC_{fines} model.

Both models are less sensitive at concentrations above about 4,000 mg/L, despite the greatest error occurring below 2,000 mg/L. As the response of the blue spectra decreases, large changes to concentrations produce small changes to DN. Qu (2014) suggests that a weaker linear relation with increasing SSC is attributed to absorption by suspended sediments; the river surface appears darker and more opaque at greater concentrations. There may be several solutions to increase model effectiveness at greater concentrations. One possible solution is to use RAW to TIF conversions with greater DN range and precision (e.g., >8-bit JPEG). Another solution may be to acquire imagery in the near-infrared spectrum, accomplished with a NIR glass filter (e.g., interference <720 nm) or permanent removal of the UV-NIR interference filters in front of a DSLR sensor.

These results warrant continued investigation and refinement of our methods. Due to the nature of regression analysis, our empirical models are likely applicable only to waters with similar characteristics such as sediment composition.

Future work will investigate the applicability of our method to other river reaches and basins, as well as to additional camera systems. Deployment of a stationary time-lapse camera is a logical advancement to our initial feasibility study as this would provide time-series information and test the system in an operational environment. These methods may provide opportunities for rapid deployment of remote camera systems at sites not suitable for in situ equipment. If paired with concurrent turbidity data, automated processing of time-lapse imagery could feed a simple piecewise defined function, to select among turbidity-SSC regressions tuned to particle size classes. Such tuning could significantly increase the accuracy of record computation at sites known to experience hysteresis in the relationship between turbidity and SSC.

CONCLUSION

Our 6-month-long study evaluated the feasibility of estimating the concentration of fine sediment (clay to silt) and total suspended sediment using close-range remote sensing imagery of a river surface acquired with an off-the-shelf consumer-grade camera system. Two empirical simple linear regression models were developed from three-band imagery and concurrent physical sample pairs (n=33, 250–7339 mg/L). Results show statistically significant relationships (90% of variability explained) between the maximum pixel value (i.e., uncalibrated digital number) of the blue band (peak response at 470 nm) and suspended-sediment concentration response variables with mean errors of 10–15%.

Standard USGS sample-based methods of generating time-series records of suspended-sediment concentration and discharge can be time- and cost-prohibitive for some studies. Although near real-time application of turbidity-based regression models may overcome these restrictions, temporal variability in suspended particle size (fines in particular) can increase uncertainty due to hysteresis. The non-contact approach we present here can mitigate some of this uncertainty by providing near real-time estimates of fines in suspension. In addition, our method can directly estimate total suspended concentration without subjecting the sensor to environmental fouling, burial, or damage during high-streamflow events.

Integration of multiple geospatial tools is becoming commonplace in river science. Despite the limited scope of this study, our results make a significant contribution in the field of river remote sensing. This method provides a consistent and straightforward procedure to quantify suspended sediment in a river using a consumer-grade digital camera. Upon further investigation and refinement, imagery-based regression models could increase the accuracy of real-time estimates of concentration, which are vital to sediment-program cooperators dependent on these data.

ACKNOWLEDGEMENTS

REFERENCES

Anderson, C.W. (2005). "Turbidity (ver. 2.1)," U.S. Geological Survey Techniques of Water-Resources Investigations, book 9, chap. A6, section 6.7, 64 p.

Curran, P.J., and Novo, E.M.M. (1988). "The relationship between suspended sediment concentration and remotely sensed spectral radiance: a review," Journal of Coastal Research, 4(3), pp 351–368.

Curtis, J.A., Flint, L.E., Alpers, C.N., Wright, S.A., and Snyder, N.P. (2006). "Use of sediment rating curves and optical backscatter data to characterize sediment transport in the upper Yuba River watershed, California, 2001–03," U.S. Geological Survey Scientific Investigations Report 2005–5246, 74 p.

Davis, B.E. (2005). "A guide to the proper selection and use of Federally approved sediment and water-quality samplers," U.S. Geological Survey Open-File Report 2005–1087, 20 p.

Duan, N. (1983). "Smearing estimate: A non-parametric retransformation method," Journal of the American Statistical Association, 78(383), pp 605–610.

Edwards, T.K., and Glysson, G.D. (1999). "Field methods for measurement of fluvial sediment," U.S. Geological Survey Techniques of Water-Resources Investigations, book 3, chap. C2, 89 p.

Gin, K.Y.H., Koh, S.T., and Lin I.I. (2003). "Spectral irradiance profiles of suspended marine clay for the estimation of suspended sediment concentration in tropical waters," International Journal of Remote Sensing, 24(16), pp 3,235–3,245.

Glysson, G.D. (1987). "Sediment transport curves," U.S. Geological Survey Open-File Report 87–218, 53 p.

Gray, J.R., Glysson, G.D., and Edwards, T.E. (2008). "Suspended-sediment samplers and sampling methods," in Garcia, Marcelo, ed., Sedimentation engineering – Processes, measurements, modeling, and practice, American Society Civil Engineers Manual 110, chap. 5.3, pp 320–339.

Gray, J.R., and Gartner, J.W. (2009). "Technological advances in suspended-sediment surrogate monitoring," Water Resources Research, 45(4), 20 p.

Guy, H.P. (1969). "Laboratory theory and methods for sediment analysis," U.S. Geological Survey Techniques of Water-Resources Investigations, book 5, chap. C1, 64 p.

Helsel, D.R., and Hirsch, R.M. (2002). "Statistical methods in water resources: hydrologic analysis and interpretation," U.S. Geological Survey Techniques of Water-Resources Investigations, book 4, chap. A3, 510 p.

Islam, M.R., Yamaguchi, Y., and Ogawa, K. (2001). "Suspended sediment in the Ganges and Brahmaputra River in Bangladesh: observation from TM and AVHRR data," Hydrological Processes, 15(3), pp 493–509.

Landers, M.N., Arrigo, J., and Gray, J.R. (2012). "Advancing hydroacoustic technologies for sedimentology research and monitoring," Eos Transactions American Geophysical Union, 93(26), p 244.

Landers, M.N., and Sturm, T.W. (2013). "Hysteresis in suspended sediment to turbidity relations due to changing particle size distributions," Water Resources Research, 49(9), pp 5,487–5,500.

Lee, C.J., Rasmussen, P.P., and Ziegler, A.C. (2008). "Characterization of suspended-sediment loading to and from John Redmond Reservoir, east-central Kansas, 2007–08," U.S. Geological Survey Scientific Investigations Report 2008–5123, 25 p.

Lewis, J. (1996). "Turbidity-controlled suspended sediment sampling for runoff-event load estimation," Water Resources Research, 32(7), pp 2,299–2,310.

Lipman, P.W., and Mullineaux, D.R., eds. (1981). "The 1980 eruptions of Mount St. Helens, Washington," U.S. Geological Survey Professional Paper 1250, 844 p.

Lodhi, M.A., Rundquist, D.C., Han, L., and Kuzila, M.S. (1997). "The potential for remote sensing of loess soils suspended in surface waters," Journal of the American Water Resources Association, 33(1), pp 111–117.

Marcus, W.A., and Fonstad, M.A. (2010). "Remote sensing of rivers: the emergence of a subdiscipline in the river sciences," Earth Surface Processes and Landforms, 35(15), pp 1867–1872.

Mertes, L.A.K., Smith, M.O., and Adams, J.B. (1993). "Estimating suspended sediment concentrations in surface waters of the Amazon River wetlands from Landsat images," Remote Sensing of the Environment, 43, pp 281–301.

Nolan, K.M., Gray, J.R., and Glysson, G.D. (2005). "Introduction to suspended-sediment sampling," U.S. Geological Survey Scientific Investigations Report 2005–5077, CD-ROM.

Porterfield, G. (1972). "Computation of fluvial-sediment discharge," U.S. Geological Survey Techniques of Water Resources Investigations, book 3, chap. C3, 66 p.

Profilocolore Sri (2013). "Variant full range on Nikon cameras: hardware and software make the system measure reflectance and spectra," Nikon experience, website accessed August 2014 at *http://www.profilocolore.com/pubblicazioni-2*

Qu, L. (2014). "Remote sensing suspended sediment concentration in the Yellow River," Ph.D. dissertation paper 383, University of Connecticut, website accessed December 2014 at *http://digitalcommons.uconn.edu/dissertations/383/.*

Rasmussen, P.P., Gray, J.R., Glysson, G.D., and Ziegler, A.C. (2009). "Guidelines and procedures for computing time-series suspended-sediment concentrations and loads from in-stream turbitiy-sensor and streamflow data," U.S. Geological Survey Techniques and Methods, book 3, chap. C4, 53 p., http://pubs.usgs.gov/tm/tm3c4/

Topping, D.J., Rubin, D.M., Wright, S.A., and Melis, T.S. (2011). "Field evaluation of the error arising from inadequate time averaging in the standard use of depth-integrating suspended-sediment samplers," U.S. Geological Survey Professional Paper 1774, 95 p.

Uhrich, M.A., and Bragg, H.M. (2003). "Monitoring in-stream turbidity to estimate continuous suspended-sediment loads and yields and clay-water volumes in the Upper North Santiam River Basin, Oregon, 1998–2000," U.S. Geological Survey Water-Resources Investigations Report 03–4098, 43 p.

Uhrich, M.A., Kolasinac, J., Booth, P.L., Fountain, R.L., Spicer, K.R., and Mosbrucker, A.R. (2014). "Correlations of turbidity to suspended-sediment concentration in the Toutle River basin, near Mount St. Helens, WA, 2010–11," U.S. Geological Survey Open-File Report 2014–1204, 30 p.

U.S. Geological Survey (2014). Branch of Quality Systems: Sediment Laboratory Quality Assurance
     Project, website accessed October 2014 at *https://bqs.usgs.gov/slqa/index.html*.
Walling, D.E. (1977). "Assessing the accuracy of suspended sediment rating curves for a small basin," Water
     Resources Research, 13(3), pp 531–538.
Wang, J.J., and Lu, X.X. (2010). "Estimation of suspended sediment concentrations using Terra MODIS: an
     example from the Lower Yangtze River, China," Science of the Total Environment, 408(5), pp 1,131–1,138.
Wang, J.J., Lu, X.X., Liew, S.C., and Zhou, Y. (2010). "Remote sensing of suspended sediment concentrations of
     large rivers using multi-temporal MODIS images: an example in the Middle and Lower Yangtze River,
     China," International Journal of Remote Sensing, 31(4), pp 1,103–1,111.
Wang, J.J., Lu, X.X., Liew, S.C., and Zhou, Y. (2009). "Retrieval of suspended sediment concentrations in large
     turbid rivers using Landsat ETM+: an example from the Yangtze River, China," Earth Surface Processes and
     Landforms, 34(8), pp 1,082–1,092.